Plasmoelectric potentials in metal nanostructures

Matthew T. Sheldon,[1] Jorik van de Groep,[2] Ana M. Brown,[1] Albert Polman,[2] Harry A. Atwater[1]*

[1]Thomas J. Watson Laboratories of Applied Physics, California Institute of Technology, MC 128-95, Pasadena, CA 91125, USA. [2]Center for Nanophotonics, FOM Institute AMOLF, Science Park 104, 1098 XG Amsterdam, Netherlands.

*Corresponding author. E-mail: haa@caltech.edu

The conversion of optical power to an electrical potential is of general interest for energy applications, and is typically obtained via optical excitation of semiconductor materials. Here, we introduce a new method using an all-metal geometry, based on the plasmon resonance in metal nanostructures. In arrays of Au nanoparticles on an indium-tin-oxide substrate and arrays of 100-nm-diameter holes in 20-nm-thick Au films on a glass substrate, we show negative and positive surface potentials during monochromatic irradiation at wavelengths below or above the plasmon resonance respectively. We observe such plasmoelectric surface potentials as large as 100 mV under 100 mW/cm^2 illumination. Plasmoelectric devices may enable development of entirely new types of all-metal optoelectronic devices that can convert light into electrical energy.

Noble metal nanostructures display remarkable optical properties that arise from the coupling of incident light to the collective motion of the conduction electrons. The excitation, propagation and localization of these plasmons can be tailored by nanoscale control of metal size and shape (*1*). Metal nanostructures exhibiting subwavelength optical confinement (*2*) have enabled nanoscale photonic waveguides, modulators, enhancement of second harmonic generation, light trapping structures for photovoltaics, and biological labeling techniques (*1*, *2*). Coupling of laser light to plasmonic structures can also result in efficient localized heating, because the resonant absorption cross section for plasmonic nanostructures is much larger than their physical cross section.

Recent work has demonstrated control over the plasmon resonance frequency (ω_p) of metal nanostructures when an external electrostatic field alters the carrier density in the metal (*3*). Increasing the carrier density in a noble metal nanoparticle leads to a blueshift of the resonance, while decreasing it leads to a redshift, as illustrated for a 20-nm-diameter Ag nanoparticle in vacuum (Fig. 1). Interestingly, the reverse effect, the optical generation of an electrostatic potential due to an optically driven change in carrier density in a plasmonic nanostructure has so far not been observed. Thermodynamically, however, such a plasmoelectric effect is expected to occur. We demonstrate direct experimental evidence of plasmoelectric potentials in the range 10-100 mV on colloidal assemblies and plasmonic light harvesting device geometries, in qualitative agreement with a thermodynamic model. These results may provide a new route to convert optical energy into electrical power.

Figure 2A shows the measured scattering spectrum for 60 nm Au colloids on ITO/glass, showing a clear plasmon resonance around λ = 550 nm. Kelvin probe force microscopy (KPFM) (*4*) with a conductive AFM tip in noncontact mode was used to probe the local static potential difference between the tip and sample surface at room temperature (Fig. 2). While the illumination wavelength is gradually scanned through the plasmon resonance spectrum, from 480-650 nm (~1 nm s^{-1}), we probe the potential on the illuminated Au nanoparticle array (*5*). A clear optically induced surface potential is observed, that varies with illumination wavelength (Fig. 2B). We observe negative induced potentials during excitation to the blue side of the neutral-particle plasmon resonance wavelength near 550 nm, and positive potentials during excitation on the red side of the resonance, with the measured potential changing sign near the peak of the plasmon resonance.

To model the experimentally observed plasmoelectric effect we consider a metal nanostructure placed on a grounded conducting substrate that is illuminated with monochromatic radiation at a wavelength just below the plasmon resonance λ_p. Random charge fluctuations between particle and substrate will cause the plasmon resonance spectrum to vary by minute amounts (Fig. 1). If an electron is randomly added to the particle, the resonance will blueshift, leading to a concomitant increase in light absorption of the particle, which in turn leads to a small increase in the nanoparticle temperature. The changes in number of electrons N and temperature $T(N)$ change the free energy F of the particle, and an equilibrium charge density is achieved when the free energy is minimum:

$$\frac{\partial F(N,T)}{\partial N} = \left(\frac{\partial F}{\partial N}\right)_T + \left(\frac{\partial F}{\partial T}\right)_N \frac{dT}{dN} = 0 \qquad (1)$$

Here, we assume that both the intensity and wavelength of the illumination is constant. Using, by definition, $(\partial F/\partial N)_T \equiv \mu$, with μ the electrochemical potential, and $-(\partial F/\partial T)_N \equiv S$, with S the entropy of the particle, we find:

$$\mu = S\frac{dT}{dN} \qquad (2)$$

Equation 2 shows that under illumination the plasmonic particle adopts a electrochemical potential that is proportional to dT/dN. This quantity, which is only determined by the plasmon resonance spectrum and the heat flow from the particle to the substrate, provides the unique thermodynamic driving force in this system. It favors charge transfer to or from the particle that increases absorption, and thereby temperature, in order to lower the free energy. The factor dT/dN is largest on the steepest parts of the resonance spectrum; it is positive for irradiation on the blue side of the resonance, leading to a positive chemical potential for the electrons, and hence a negative voltage; the reverse is observed for irradiation on the red side of the resonance. All these trends are exactly as observed in the experimental spectra of Fig. 2B: the surface potential vanishes at the peak of the resonance where dT/dN is zero; the largest (negative) potential is observed at a wavelength of 500 nm, coinciding with the steepest slope in the resonance spectrum of Fig. 2A.

Equation 1 can be used to quantitatively estimate the equilibrium plasmoelectric potential, writing $F(N, T)$ as the sum of the free energies of electrons and phonons, using the well-known free energy functions of an electron and phonon gas (*6*, *7*). The electronic term is composed of a contribution due to the chemical potential of the electrons that is directly given by the Fermi function, and an electrostatic contribution due to charging of the metal nanosphere; the phonon term is given by the Debye model. Taking the derivatives to N and T we find analytical expressions for $\mu(N, T)$ and $S(N, T)$, that are then input in Eq. 2 (*5*).

Before applying the model to the experimental geometry in Fig. 2 we calculate the plasmoelectric potential, i.e., the electrochemical potential gained by the particle from the electron transfer induced by optical absorption, for a spherical 20-nm-diameter Ag nanoparticle in vacuum under monochromatic illumination. For these particles analytical Mie theory can be used to calculate the absorption cross section spectrum, $C_{\mathrm{abs}}(\lambda, n)$, for a given electron density in the nanoparticle, by taking into account the dependence of the bulk plasma frequency, ω_p, in the complex dielectric function of the metal on carrier density, $\omega_p \propto n^{1/2}$ (*5*). To calculate the nanoparticle temperature, we use a steady-state heat-flow model in which heat is dissipated from the nanoparticle by radiation. Figure 3A shows the calculated plasmoelectric potential of the Ag nanoparticle as a function of illumination wavelength at an incident flux of 1 $\mathrm{mW/cm^2}$, under which the particle obtains a maximum temperature of ~400 K (*5*). The model predicts a clear negative surface potential below the plasmon resonance and a positive one, up to 150 mV, above it. The asymmetry in the plasmoelectric potential below and above the resonance wavelength is due to the intrinsic non-resonant interband absorption in the metal. Figure 3B shows the corresponding relative absorption increase for the Ag nanoparticle, it ranges up to 2.5×10^{-5}.

The model for the simple geometry in Fig. 3 describes the key factors in the plasmoelectric effect: an increase in carrier density under illumination at wavelengths shorter than the resonance peak, inducing a negative plasmoelectric potential and enhanced absorption compared with the neutral particle. Similarly, radiation at longer wavelengths induces a lower carrier density, a positive plasmoelectric potential, and enhanced absorption. These results demonstrate that an excited plasmonic resonator behaves as a heat engine that can convert absorbed off-resonant optical power into a static electrochemical potential.

Next, we use the model to calculate the wavelength-dependent and power-dependent plasmoelectric potential for the experimental geometry in Fig. 2, a spherical 60-nm-diameter Au particle on an ITO/glass substrate. We calculated the factor dT/dN in Eq. 2 using Finite-Difference Time-Domain (FDTD) simulations of the absorption spectra for an Au particle on an ITO/glass substrate to take into account radiative damping from the substrate not captured by simple Mie theory and a 1D model for heat conduction into the substrate (*5*). Due to variations in interparticle coupling and clustering (see SEM in Fig. 2A), and possible adsorption of water on the particle-ITO interface, the ensemble dielectric environment is complex. The broadened, red-shifted scattering spectrum in Fig. 2A is evidence for some particle aggregation. In the FDTD simulations we model these effects by assuming a background index of $n = 1.4$ for the medium above the ITO substrate, such that the absorption spectrum matches the experimentally observed spectrum. As can be seen in Fig. 2C for the high-power data, the modeled trends correspond well with the experimental trends: the modeled minimum potential occurs at 530 nm (experimental: 500 nm), the modeled zero potential at 545 nm (experimental: 560 nm), and a large positive potential is observed for wavelengths above the resonance, both in model and experiment. The extent of the measured potential to wavelengths up to 640 nm in Fig. 2B is in agreement with the long-wavelength tail in the spectrum of Fig. 2A. At 555 nm the modeled particle temperature peaks at 308 K, 15 K above ambient (*5*), in good agreement with other experimental observations (*8*).

To aid interpretation of our findings, we comment briefly on other mechanisms for generating photopotentials with metals. A thermoelectric effect is several orders of magnitude weaker ($\sim\mu\mathrm{V}\ \Delta\mathrm{K}^{-1}$) than the observed potentials (*9*). Hot-carrier induced effects would require rectifying contacts which are not present in our geometry. Moreover, both these effects would not result in a bisignated signal (*10*). "Plasmon drag" or similar direct photon-to-electron momentum transfer mechanisms on Au colloids would not produce a bisignated signal; nor for the symmetric hole arrays described below under normal-incidence irradiation (*11*). Future work will focus on obtaining further insight in the microscopic mechanisms that contribute to the observed effect.

To demonstrate the generality of the observed plasmoelectric effect we measured the plasmoelectric potential on 10-micron-sized arrays of subwavelength holes in an optically thin Au film on a glass substrate. In these microarrays, light is absorbed by the resonant excitation of interacting surface plasmon polaritons that propagate between the holes on the Au-air and Au-glass interface (*5*, *12*). The absorption spectrum of a single array is determined by the coherent interaction of plasmons within the array, and the study of such arrays thus enables probing the plasmoelectric effect on a single absorber geometry. Moreover, the metal hole array architectures provide a first step toward future plasmoelectric integrated circuitry in which plasmoelectric power is harvested.

Figure 4, A and B, shows a fabricated 10 × 10-μm hole array composed of 100-nm-diameter holes in a square array with a pitch of 200 nm, made in a 20-nm-thick Au film on a glass substrate. Figure 4C shows the measured absorption spectra of hole arrays with a pitch of 175 – 300 nm (*5*). Increasing the pitch leads to a clear redshift in the absorption spectrum. Figure 4D shows the corresponding measured surface potential as a function of the wavelength of illumination ($100\ \mathrm{mW\ cm^{-2}}$), as measured with KPFM. A transition from negative to positive surface potential is seen for each array geometry. Also, the measured potential spectra show a clear redshift with increasing array pitch, in accordance with the trend in the absorption spectra. The maximum plasmoelectric potential observed for each measurement shows a gradually decreasing trend with increasing pitch, also in agreement with the trend in the absorption spectra. A slight difference is observed between the zero-crossing in the potential measurements and the peak in the corresponding absorption spectrum, which is attributed to the difference in numerical aperture (NA) of the microscope objective used for the two measurements (*5*). All surface potential spectra show clear minima and maxima and then decrease as the wavelength is tuned further away from the resonance, as expected. The measurements in Fig. 4D show a plasmoelectric potential as large as ±100 mV and demonstrate the generality of the plasmoelectric effect for arbitrary plasmonic absorbers.

The observed plasmoelectric phenomenon takes advantage of the remarkable spectral tailorability of plasmonic nanostructures and can be extended to a variety of material systems, absorber geometries, and radiation environments. Plasmoelectric devices may enable development of entirely new types of all-metal optoelectronic devices that can convert light into electrical energy by replacing the usual function of doped semiconductors with metal nanostructures that are optically excited off-resonance.

References and Notes

1. J. A. Schuller, E. S. Barnard, W. Cai, Y. C. Jun, J. S. White, M. L. Brongersma, Plasmonics for extreme light concentration and manipulation. *Nat. Mater.* **9**, 193–204 (2010). Medline doi:10.1038/nmat2630
2. L. Novotny, N. van Hulst, Antennas for light. *Nat. Photonics* **5**, 83–90 (2011). doi:10.1038/nphoton.2010.237
3. C. Novo, A. M. Funston, A. K. Gooding, P. Mulvaney, Electrochemical charging of single gold nanorods. *J. Am. Chem. Soc.* **131**, 14664–14666 (2009). Medline doi:10.1021/ja905216h
4. M. Nonnenmacher, M. P. O'Boyle, H. K. Wickramasinghe, Kelvin probe force microscopy. *Appl. Phys. Lett.* **58**, 2921 (1991). doi:10.1063/1.105227
5. See supplementary materials on *Science* Online.
6. N. W. Ashcroft, N. D. Mermin, *Solid State Physics* (Harcourt, New York, 1976).
7. B. M. Askerov, S. Figarova, Thermodynamics, Gibbs Method and Statistical Physics of Electron Gases (Springer, New York, 2010).
8. M. G. Cerruti, M. Sauthier, D. Leonard, D. Liu, G. Duscher, D. L. Feldheim, S. Franzen, Gold and silica-coated gold nanoparticles as thermographic labels

for DNA detection. *Anal. Chem.* **78**, 3282–3288 (2006). Medline doi:10.1021/ac0600555

9. F. J. Blatt, P. A. Schroeder, C. F. Foiles, *Thermoelectric Power of Metals* (Plenum, New York, 1976).
10. M. W. Knight, H. Sobhani, P. Nordlander, N. J. Halas, Photodetection with active optical antennas. *Science* **332**, 702–704 (2011). Medline doi:10.1126/science.1203056
11. N. Noginova, A. V. Yakim, J. Soimo, L. Gu, M. A. Noginov, Light-to-current and current-to-light coupling in plasmonic systems. *Phys. Rev. B* **84**, 035447 (2011). doi:10.1103/PhysRevB.84.035447
12. W. L. Barnes, W. A. Murray, J. Dintinger, E. Devaux, T. W. Ebbesen, Surface plasmon polaritons and their role in the enhanced transmission of light through periodic arrays of subwavelength holes in a metal film. *Phys. Rev. Lett.* **92**, 107401 (2004). Medline doi:10.1103/PhysRevLett.92.107401
13. E. D. Palik, *Handbook of Optical Constants of Solids* (Academic Press, New York, 1985).
14. A. D. Rakic, A. B. Djurisic, J. M. Elazar, M. L. Majewski, Optical properties of metallic films for vertical-cavity optoelectronic devices. *Appl. Opt.* **37**, 5271–5283 (1998). Medline doi:10.1364/AO.37.005271
15. G. V. Hartland, Optical studies of dynamics in noble metal nanostructures. *Chem. Rev.* **111**, 3858–3887 (2011). Medline doi:10.1021/cr1002547
16. S. A. Maier, *Plasmonics: Fundamentals and Applications* (Springer, New York, 2007).
17. J. M. Luther, P. K. Jain, T. Ewers, A. P. Alivisatos, Localized surface plasmon resonances arising from free carriers in doped quantum dots. *Nat. Mater.* **10**, 361–366 (2011). Medline doi:10.1038/nmat3004
18. G. Garcia, R. Buonsanti, E. L. Runnerstrom, R. J. Mendelsberg, A. Llordes, A. Anders, T. J. Richardson, D. J. Milliron, Dynamically modulating the surface plasmon resonance of doped semiconductor nanocrystals. *Nano Lett.* **11**, 4415–4420 (2011). Medline doi:10.1021/nl202597n
19. J. Gordon II, S. Ernst, Surface-plasmons as a probe of the electrochemcial interface. *Surf. Sci.* **101**, 499–506 (1980). doi:10.1016/0039-6028(80)90644-5
20. K. F. MacDonald, Z. L. Sámson, M. I. Stockman, N. I. Zheludev, Ultrafast active plasmonics. *Nat. Photonics* **3**, 55–58 (2009). doi:10.1038/nphoton.2008.249
21. V. Palermo, M. Palma, P. Samorì, Electronic characterization of organic thin films by Kelvin probe force microscopy. *Adv. Mater.* **18**, 145–164 (2006). doi:10.1002/adma.200501394
22. W. Shockley, H. J. Queisser, Detailed balance limit of efficiency of p-n junction solar cells. *J. Appl. Phys.* **32**, 510–519 (1961). doi:10.1063/1.1736034
23. C. Kittel, *Introduction to Solid State Physics* (Wiley, New York, ed. 8, 2005).
24. P. T. Landsberg, G. Tonge, Thermodynamic energy conversion efficiencies. *J. Appl. Phys.* **51**, R1–R20 (1980). doi:10.1063/1.328187
25. J. P. Holman, *Heat Transfer* (McGraw-Hill, New York, ed. 10, 2009).
26. N. D. Lang, W. Kohn, Theory of metal surfaces: Induced surface charge and image potential. *Phys. Rev. B* **7**, 3541–3550 (1973). doi:10.1103/PhysRevB.7.3541
27. T. Sannomiya, H. Dermutz, C. Hafner, J. Vörös, A. B. Dahlin, Electrochemistry on a localized surface plasmon resonance sensor. *Langmuir* **26**, 7619–7626 (2010). Medline doi:10.1021/la9042342
28. P. B. Johnson, R. W. Christy, Optical constants of the noble metals. *Phys. Rev. B* **6**, 4370–4379 (1972). doi:10.1103/PhysRevB.6.4370
29. B. Luk'yanchuk, N. I. Zheludev, S. A. Maier, N. J. Halas, P. Nordlander, H. Giessen, C. T. Chong, The Fano resonance in plasmonic nanostructures and metamaterials. *Nat. Mater.* **9**, 707–715 (2010). Medline doi:10.1038/nmat2810
30. FDTD Solutions, Lumerical Solutions Inc., Vancouver, BC, Canada; www.lumerical.com.
31. J. Parsons, E. Hendry, C. Burrows, B. Auguié, J. Sambles, W. Barnes, Localized surface-plasmon resonances in periodic nondiffracting metallic nanoparticle and nanohole arrays. *Phys. Rev. B* **79**, 073412 (2009). doi:10.1103/PhysRevB.79.073412
32. J. Braun, B. Gompf, G. Kobiela, M. Dressel, How holes can obscure the view: Suppressed transmission through an ultrathin metal film by a subwavelength hole array. *Phys. Rev. Lett.* **103**, 203901 (2009). Medline doi:10.1103/PhysRevLett.103.203901
33. R. W. Alexander, G. S. Kovener, R. J. Bell, Dispersion curves for surface electromagnetic waves with damping. *Phys. Rev. Lett.* **32**, 154–157 (1974). doi:10.1103/PhysRevLett.32.154
34. G. S. Kovener, R. W. Alexander Jr., R. J. Bell, Surface electromagnetic waves with damping. I. Isotropic media. *Phys. Rev. B* **14**, 1458–1464 (1976). doi:10.1103/PhysRevB.14.1458
35. A. F. Koenderink, A. Polman, Complex response and polariton-like dispersion splitting in periodic metal nanoparticle chains. *Phys. Rev. B* **74**, 033402 (2006). doi:10.1103/PhysRevB.74.033402
36. T. W. Ebbesen, H. J. Lezec, H. F. Ghaemi, T. Thio, P. A. Wolff, Extraordinary optical transmission through sub-wavelength hole arrays. *Nature* **391**, 667–669 (1998). doi:10.1038/35570

Acknowledgments: The authors gratefully acknowledge support from the Department of Energy, Office of Science under grant DE-FG02-07ER46405 (MS and HAA) and for facilities of the DOE "Light-Material Interactions in Energy Conversion" Energy Frontier Research Center (DE-SC0001293). Work at AMOLF is part of the research program of the Foundation for Fundamental Research on Matter, which is financially supported by the Netherlands Organization for Scientific Research (NWO). It is also supported by the European Research Counsel. One of us (AB) acknowledges support from an NSF Graduate Research Fellowship. The data are archived in the laboratory of HAA. Helpful discussions with E. Kosten, V. Brar, D. Callahan, M. Deceglie, A. Leenheer, J. Fakonas, R. van Roij, B.M. Mulder and H.J. Bakker are gratefully acknowledged.

Supplementary Materials
www.sciencemag.org/cgi/content/full/science.1258405/DC1
Materials and Methods
Supplementary Text
Figs. S1 to S9
References (*13–36*)

7 July 2014; accepted 16 October 2014

10.1126/science.1258405

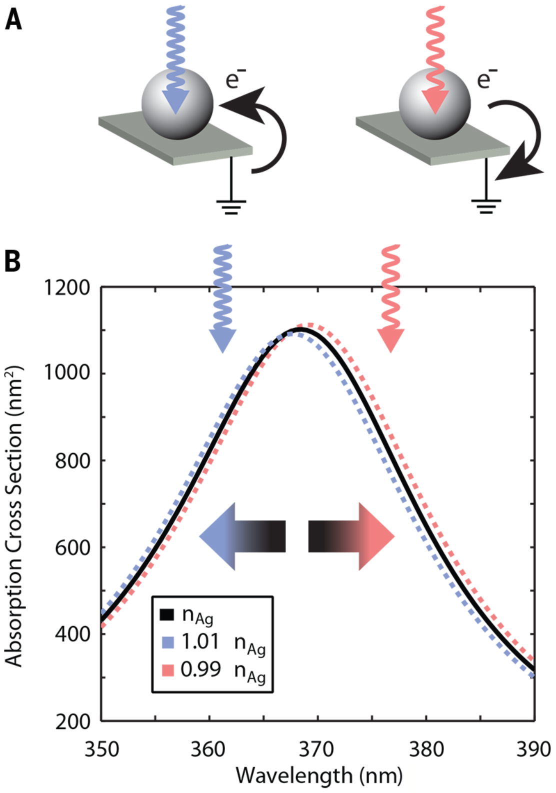

Fig. 1. Absorption cross section spectrum of a Ag nanoparticle and the plasmoelectric effect. Calculated absorption cross section for a 20-nm-diameter Ag nanoparticle in vacuum with bulk carrier density n_{Ag} and carrier densities that are reduced or increased by 1%. Schematics: Spontaneous charge transfer to or from the nanoparticle is thermodynamically favored when the consequent spectral shift increases the absorption, raising the temperature. Irradiation on the blue side of the resonance leads to a negative charge on the particle, irradiation on the red side to a positive charge.

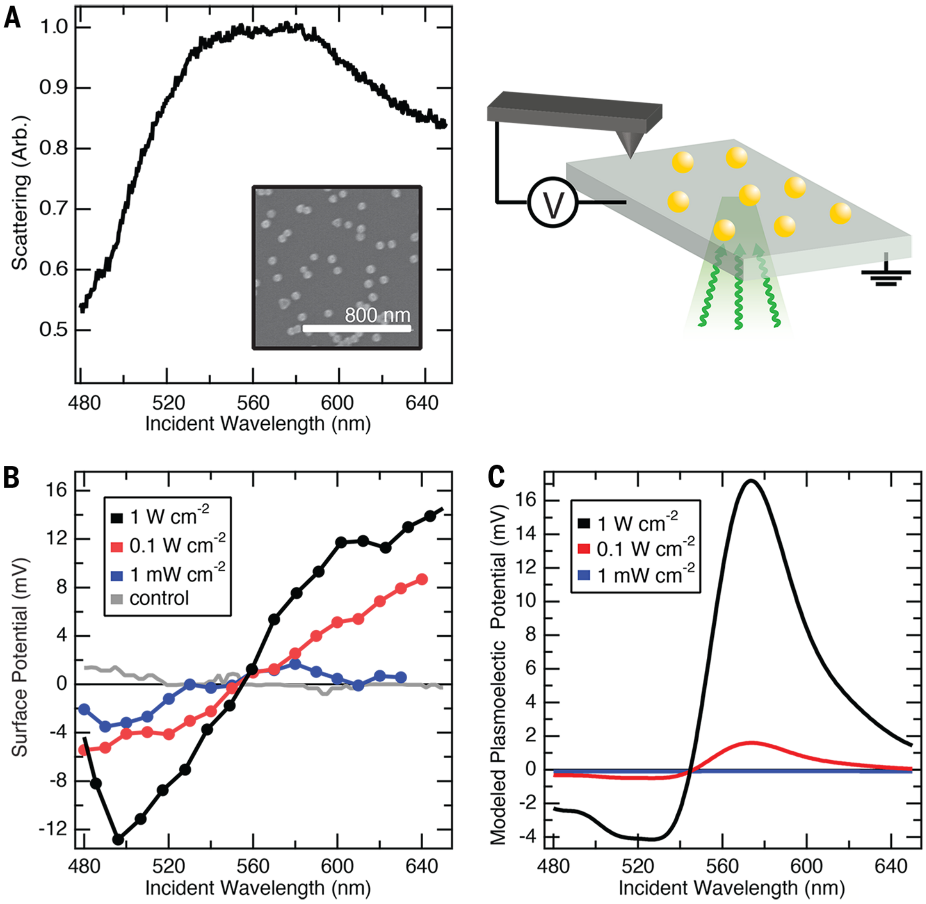

Fig. 2. Plasmoelectric effect on dense Au nanoparticle arrays on ITO/glass. (**A**) Dark-field scattering spectrum of 60-nm-diameter Au nanoparticles on ITO/glass. The inset shows an SEM image of the nanoparticle array. (**B**) Kelvin probe force microscopy measurements of the surface potential as a function of illumination wavelength (15-nm bandwidth) for three different illumination intensities. The surface potential of a flat region of ITO/glass adjacent to the nanoparticle array was monitored during scanned monochromatic illumination (see schematic geometry). A control measurement of an ITO/glass substrate without nanoparticles (1 W/cm^2) is also plotted (grey). (**C**) Modeled plasmoelectric potential for 60-nm-diameter Au nanoparticles on ITO/glass for the three illumination intensities in (B).

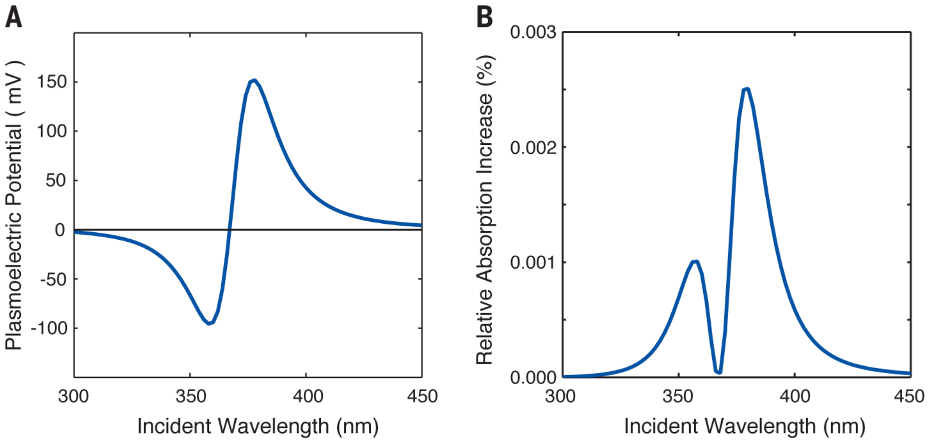

Fig. 3. Modeled plasmoelectric response for Ag nanoparticles. A 20-nm-diameter Ag particle in vacuum is illuminated with monochromatic light (1 mW/cm^2). (**A**) Plasmoelectric potential and (**B**) relative absorption increase as a function of incident wavelength.

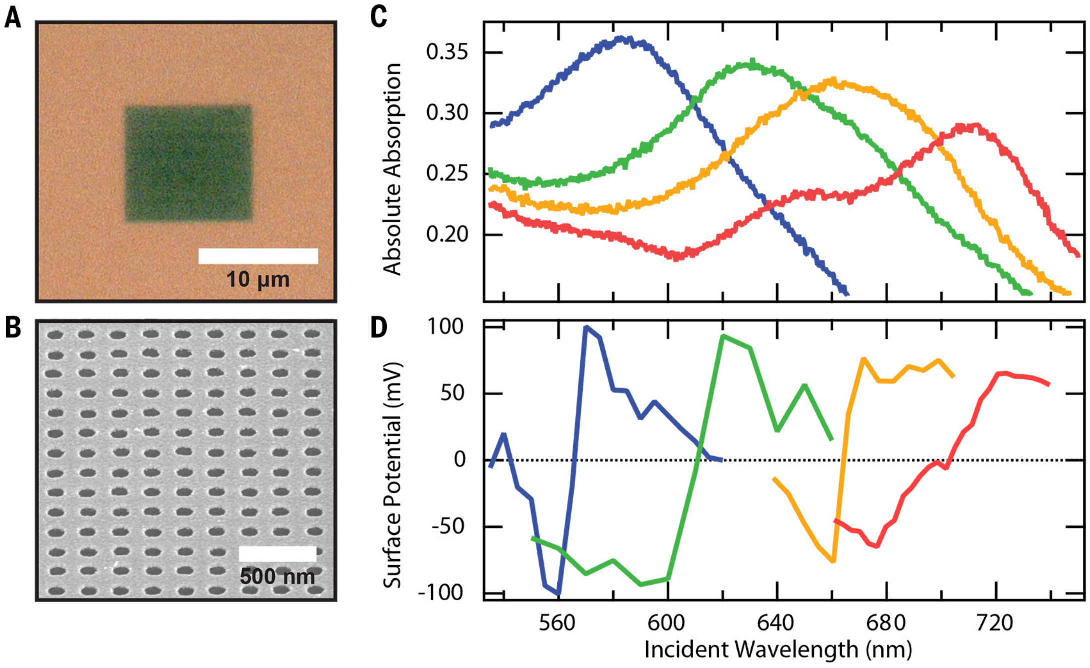

Fig. 4. Plasmoelectric effect on Au nanohole arrays on glass. (**A**) Bright-field optical microscope image showing a 200-nm-pitch array of 100-nm-diameter holes in a 20-nm-thick Au film on glass. The dark green color directly shows the strong absorption in the hole array. (**B**) SEM image of a 200-nm-pitch hole array imaged under 52 degrees with respect to the normal. (**C**) Measured optical absorption spectra for hole arrays with a pitch of 175 nm (blue), 225 nm (green), 250 nm (yellow) and 300 nm (red) (NA = 0.8). (**D**) Surface potential as a function of excitation wavelength measured using Kelvin force probe microscopy at 100 mW/cm^2 for the four hole arrays in (**C**) (NA = 0.25).